Enabling Wide Bandwidth in Substrate-Integrated Waveguide Slot Antennas by Using Low-Index Metamaterials

Amir Jafargholi,[1,*] Romain Fleury,[1] Mohammad Hossein Mazaheri,[2] and Jalaledin Tayebpour[3]

[1] *Laboratory of Wave Engineering, Ecole polytechnique fédérale de Lausanne (EPFL), CH 1015 Lausanne, Switzerland*

[2] *Department of Computer Science, University of California, Los Angeles (UCLA), Los Angeles, California 90095-1596, USA*

[3] *Department of Electrical and Computer Engineering, University of Waterloo, Waterloo, Ontario N2L 3G1, Canada*

(Received 6 September 2023; revised 30 October 2023; accepted 2 November 2023; published 11 January 2024)

This paper presents a solution to overcome the inherently limited bandwidth of substrate-integrated waveguide (SIW) slot antennas. It is analytically shown that by decreasing the permittivity of a dielectric loaded slot antenna, the resulting bandwidth increases significantly, where the widest bandwidth can be achieved when the permittivity of the dielectric is less than unity. To demonstrate this concept, a rectangular SIW slot is loaded by an array of thin wires to realize the desired low-index metamaterials (MTMs), which consequently results in a single-layer, compact, and cost-effective structure. We have measured an impedance bandwidth ($|S_{11}| < -10$ dB) of 36.2%, covering the millimeter-wave (mmWave) frequency range of 19.7–28.4 GHz. The radiation efficiency is above 90%, providing at least 7.5 decibels relative to isotropic (dBi) gain through the entire frequency band, making it a potential candidate for industrial, scientific and medical (ISM) and/or automotive radar (24.125–24.25 GHz) and 5G (24.25–28.35 GHz). Measurements show that the proposed antenna not only has a broad impedance bandwidth but also an improved radiation bandwidth.

DOI: 10.1103/PhysRevApplied.21.014017

I. INTRODUCTION

Increasing demands for high-capacity wireless communication draw the attention of engineers to the promising solutions provided by millimeter-wave (mmWave) technologies. A key element of any mmWave technology is the antenna, the role of which is to efficiently transmit and receive the signals encoded within the operating band. Among all antenna solutions, the substrate-integrated waveguide (SIW) slot antenna is one of the most commonly used antennas in mmWave applications. Besides being straightforward to fabricate, its simple structure helps engineers to design complex arrays in various configurations, while being easy to integrate into front-end circuits. These antennas can provide high radiation gain by employing slot arrays on a single-SIW structure [1]. Moreover, they have less power leakage and intrinsic loss than competing solutions based on microstrips [2].

Despite all these advantages, the bandwidth of the SIW slot antenna is limited due to its resonating nature and it does not cover the allocated frequency spectrum for 5G applications. One common technique to enhance the antenna bandwidth employs multiple slots with closeby resonant frequencies, which has enabled an increase of the fractional bandwidth up to 22.4%, at the expense of the size of the system [3]. A similar approach is to simultaneously excite two hybrid modes in a SIW cavity, reaching 11.7% bandwidth [4], or combining a multimode resonance SIW cavity with a complementary split-ring resonator, obtaining 22.2% bandwidth [5]. In these solutions, a multimodal resonance enables a wider bandwidth at the expense of increasing cross-polarization in the H plane, especially at higher frequencies. In addition, coupling with inherently broadband magnetoelectric (ME) dipoles has helped to increase the bandwidth [6,7]. However, all these solutions suffer from a large electrical size, thick dielectric substrates, and a challenge in front-end integration, as well as the fact that the radiation bandwidth is narrower than the impedance bandwidth when the element is extended into an array, which causes drastic limitations.

On the other hand, metamaterials (MTMs) have found enormous applications in antenna engineering and applied electromagnetics. MTMs exhibit anomalous electromagnetic responses that have enabled a new class of compact efficient antennas, filters, and other microwave devices [8,9]. For instance, an ϵ-negative (ENG) or μ-negative

*amir.jafargholi@epfl.ch

 © 2024 American Physical Society

material can be employed to shrink the size of an antenna [10]. Among all the types of MTMs, ϵ-near-zero (ENZ) MTMs are one of the most interesting. They have a variety of applications [11], including cloaking, radiation enhancement, energy tunneling, and compact impedance matching [12]. In antennas, they have been used not only to reduce the electrical size or improve the radiation performance [13] but also to increase the antenna gain [14–16], induce tunneling effects for greater compactness [17,18], create quasistatic modes for miniaturization [19–21], enable dual-frequency [22] or dual-polarized [23] operation, exploit superluminal behavior in waveguides [24,25] or for radiation [26–28], control the radiation characteristics [29–32], increase the isolation in MIMO [33], and induce shape insensitivity or length invariance [34–36]. All these structures, however, suffer from drastic constraints in fractional bandwidth brought about by the inherently dispersive behavior of MTMs, which limits the bandwidth of ENZ operation.

In this paper, we manage to tame such dispersive effects and take advantage of a low-index MTM to increase both the impedance and radiation bandwidths of a substrate-integrated waveguide slot antenna. Instead of targeting near-zero permittivity, we engineer an array of thin wires the effective index of refraction of which is below unity within a broader frequency band. The fabricated antenna prototype is a single-layer, compact, and low-cost SIW slot antenna with a broad impedance and radiation bandwidth. We envision that our MTM-enabled antenna design may unleash the full power of 5G and 6G technologies by enabling a simple efficient solution for emission and reception covering the entirety of the spectral bands available at mmWave frequencies.

II. BACKGROUND THEORY

To analytically study the behavior of the main problem, we investigate the input impedance of a dielectric loaded slot waveguide antenna (SWA) as a first step. It is shown that by decreasing the permittivity of the dielectric, the antenna bandwidth increases. This fact stems from the typical relationship between the permittivity and the antenna bandwidth, as expressed by BW $\propto \sqrt{\mu/\epsilon}$, [37]. While this relationship is not a universal formula for all types of antennas, the antenna bandwidth also depends on factors such as the feeding structure, substrate materials, the geometry of the radiating part, and the ground plane. Consequently, the widest bandwidth is achieved when the dielectric permittivity is less than unity. Given the intricate nature of the analytical approach for the SIW slot antenna, investigating the dielectric loaded SWA model offers valuable insights into the primary issue with reduced complexity. They behave in a similar manner; however, some discrepancies exist between the theoretically studied structure and the proposed antenna. These discrepancies arise from practical considerations, including fabrication technology.

A SWA made of a rectangular waveguide with a transverse slot on its broad wall is considered (see Fig. 1). The normalized input impedance of the slot can be written as [38]

$$Z/Z_0 = 2\Gamma/(1-\Gamma), \tag{1}$$

where Z_0 is the characteristic impedance and Γ is the reflection coefficient, defined by

$$\Gamma = \frac{\sin\left(\beta_{10}\frac{w_S}{2}\right)}{\omega\mu_0\sqrt{ab}} \sum_{p=1}^{N} \frac{E_p \frac{p\pi}{2L_S}}{\left(\frac{p\pi}{2L_S}\right)^2 - \left(\frac{\pi}{a}\right)^2} \times \begin{pmatrix} \sin\left(\frac{\pi x_0}{a}\right)\cos\left(\frac{\pi L_S}{a}\right) \\ -\cos\left(\frac{\pi x_0}{a}\right)\sin\left(\frac{\pi L_S}{a}\right) \end{pmatrix}_{p=\text{even}}^{p=\text{odd}}, \tag{2}$$

where a is the width of the broad waveguide wall, b is the narrow wall height of the waveguide, and β_{10} is the wave number of the dominant mode. The slot length is defined by $2L_S$ and its offset from the center of the waveguide is x_0, as depicted in Fig. 1. It should be noted that the field variation along the slot width w_S is neglected, since w_S is much smaller than the slot length L_S. The antenna impedance varies with frequency, as indicated in Eq. (2), and as we will shortly show, the reflection coefficient of the SWA has a sine cardinal behavior with respect to ω. As a result, the impedance bandwidth of the slot is limited to a narrow region around a particular value of β_{10}. According to Eq. (3), the wave number of the dominant propagating mode (TE_{10}) in a rectangular waveguide is in direct relation with the dielectric permittivity:

$$\begin{aligned} \beta_{mn} &= \sqrt{\omega^2\mu_0\varepsilon_0\varepsilon_r - \left(\frac{m\pi}{a}\right)^2 - \left(\frac{n\pi}{b}\right)^2}, \\ \beta_{10} &= \sqrt{\omega^2\mu_0\varepsilon_0\varepsilon_r - \left(\frac{\pi}{a}\right)^2}, \end{aligned} \tag{3}$$

which at high frequencies can be approximated by

$$\beta_{10} \approx \omega\sqrt{\mu_0\varepsilon_0\varepsilon_r}. \tag{4}$$

By substituting Eq. (4) in Eq. (2), the reflection coefficient is reduced to

$$\Gamma \approx \frac{\sin\left(\omega\sqrt{\mu_0\varepsilon_0\varepsilon_r}\frac{w_S}{2}\right)}{\omega\mu_0\sqrt{ab}} \Psi\left(a, x_0, L_S\right), \tag{5}$$

where Ψ represents the frequency-independent terms. Now, consider a rectangular waveguide with dimensions of $a = 25$ mm and $b = 0.787$ mm. Figure 2 shows the normalized input impedance of a dielectric loaded SWA

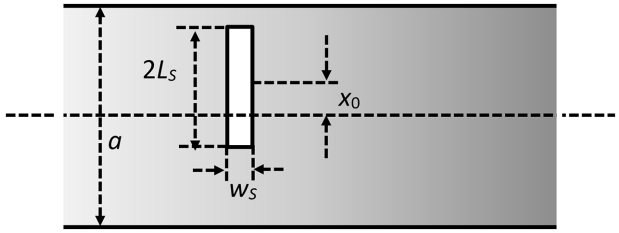

FIG. 1. A transverse slot on the broad wall of a rectangular waveguide.

calculated by Eq. (1) for different slot lengths. The resonant frequency of the antenna varies in the range of 25 GHz to 16 GHz by increasing the slot length from 8.0 mm to 14 mm. In this figure, the relative permittivity of the dielectric material is 2.33. For a 10-mm slot loaded by such material, the antenna resonates at 16.2 GHz.

By decreasing the permittivity, the numerator in Eq. (5) declines, which results in a lower reflection coefficient over a broader frequency band. Substitution of Eq. (5) in Eq. (1) shows the effect of decreasing the permittivity:

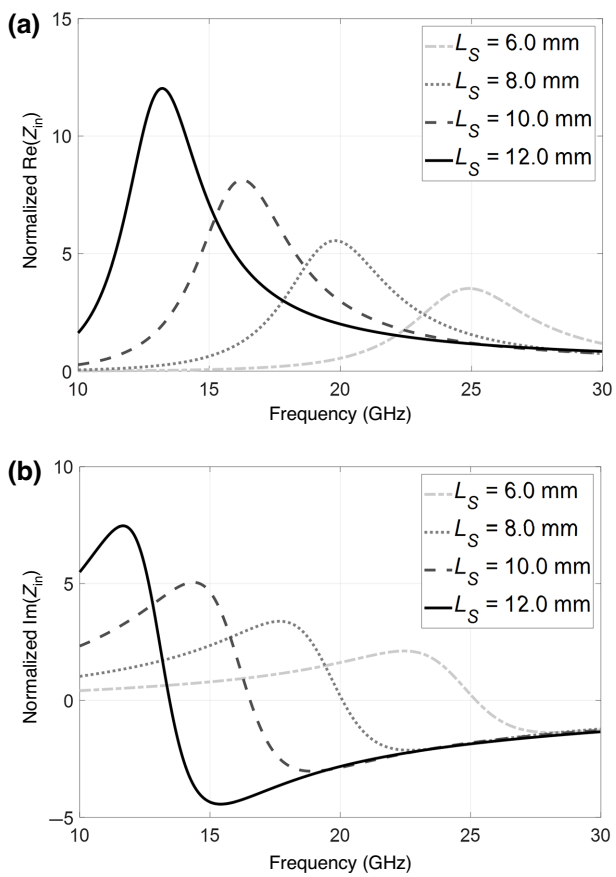

FIG. 2. The normalized input impedance (to 50 Ω) of a dielectric loaded SWA as a function of the slot length: (a) real part; (b) imaginary part.

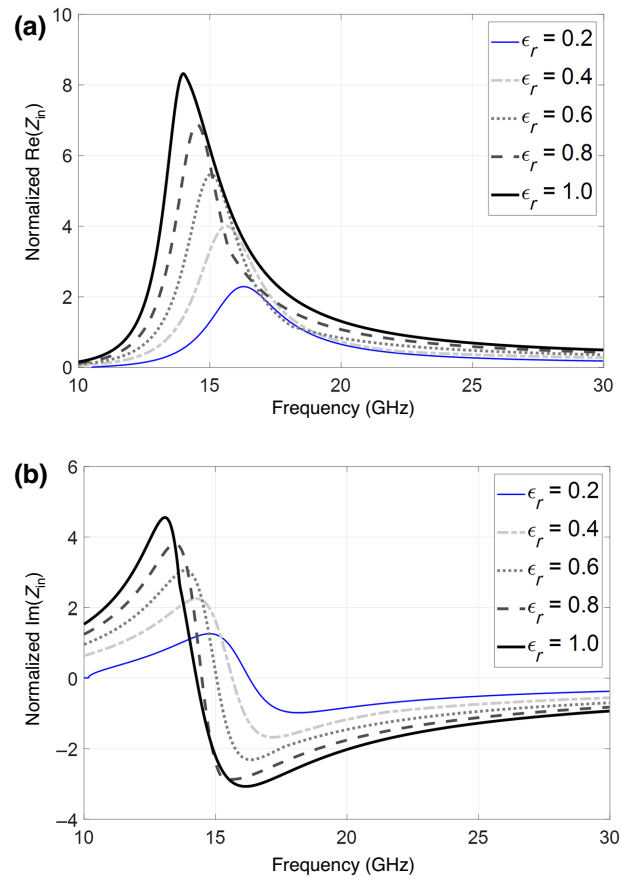

FIG. 3. The normalized input impedance (to 50 Ω) of a dielectric loaded SWA as a function of the dielectric permittivity: (a) real part; (b) imaginary part.

the real part of the input impedance gets closer to unity, while the imaginary part gets closer to zero. In the zero-permittivity limit, the imaginary part of the normalized input impedance becomes zero, while the real component reaches one. Figure 3 illustrates such a dependence of the normalized input impedance as a function of the dielectric permittivity. Note that the impedance variation over the frequency is highly reduced. This figure assumes that the slot length and width are 10 mm and 0.5 mm, respectively.

In order to examine the consequence of this effect on an antenna, an SIW slot structure is simulated numerically (see Fig. 4). To avoid any unwanted radiation from the port, an ideal bulk dielectric with a permittivity of $\epsilon_r \leq 1$ is placed just beneath the radiating part, with sufficient separation from the SIW side walls or the microstrip feed line. The Rogesrs RT/duroid® 5870 substrate, with a thickness of 0.787 mm and a relative permittivity of 2.33, is employed. The width of the feed line is designed for 50 Ω and a tapered transition is used to match the microstrip line to the SIW structure. The radius of the SIW via is 0.3 mm, with a spacing of 1.2 mm between adjacent vias. The radiating slot length is 10 mm and is symmetrically placed with

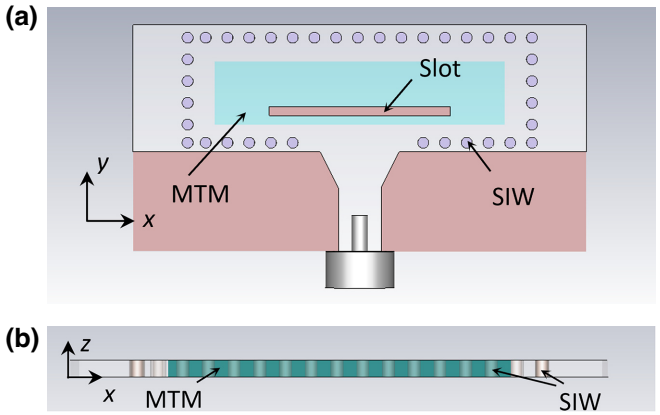

FIG. 4. A schematic of the SIW slot loaded by a homogeneous bulk of low-index MTM: (a) front view; (b) side view. The MTM is shown in cyan. The antenna parameters are labeled in Fig. 8.

regard to the x axis at the center of the SIW structure. The dimensions of the low-index bulk MTM are 16×3.5 mm^2 and its thickness is the same as that of the substrate.

The antenna is numerically simulated for different permittivity values and the results are compared in Fig. 5(a). Consistent with the above discussion, the real and imaginary parts of the input impedance decrease with the relative permittivity and the antenna bandwidth is consequently extended. Here, the results are in good agreement with our analytical considerations and the antenna bandwidth (voltage standing-wave ratio, VSWR ≤ 2) is extended by reducing the permittivity. However, realistic MTMs are inherently frequency dispersive and it is important to evaluate how this affects the bandwidth enhancement. Thus, we turn to a simple Drude model of the MTM dispersion [11]. The Drude model exhibits a broad frequency range with low-index permittivity (when the operating frequency is greater than the plasma frequency, $f \geq f_P$) and accurately describes a simple class of MTMs made of arrays of thin conducting wires. Explicitly, we assume that $\epsilon_r = 1 - [\omega_p^2/(\omega^2 + j\gamma\omega)]$, where $\omega_p = 2\pi f_P$ is the plasma frequency and γ is the electric damping or collision frequency. The antenna VSWR as a function of ω_p (the plasma frequency) is presented in Fig. 5(b). The numerical simulations show a behavior similar to that of the nondispersive case; however, the bandwidth is restricted accordingly and the antenna operating-frequency range is determined by several parameters that will be studied in Sec. III.

III. ANTENNA DESIGN

A. Cell design

Low-index materials can be found in the visible and infrared parts of the electromagnetic spectrum but not at lower frequencies. Therefore, at microwave frequencies,

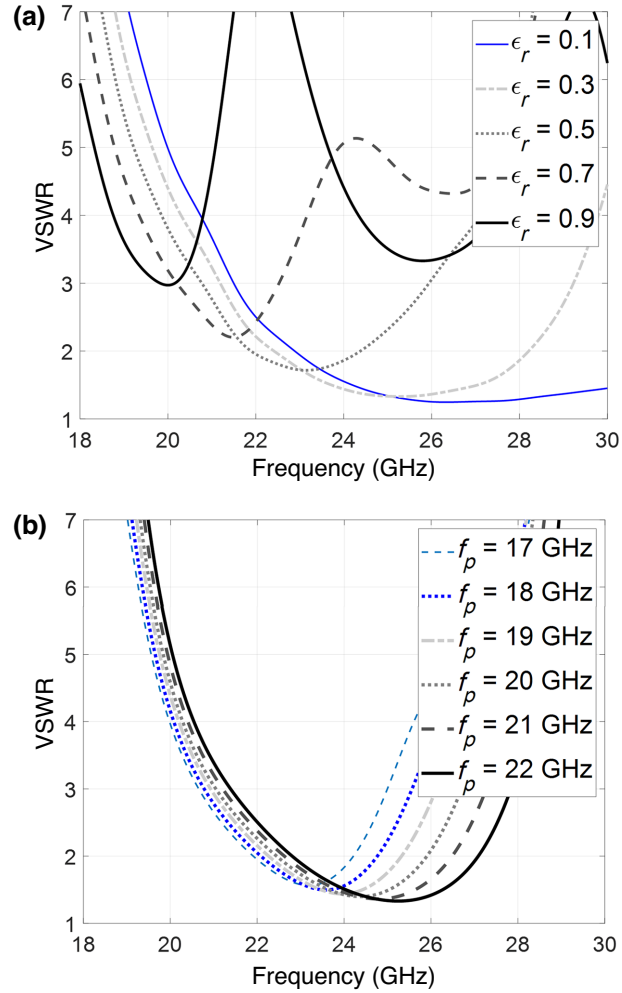

FIG. 5. The antenna VSWR for different (a) permittivities and (b) plasma frequencies.

they are typically implemented with MTMs such as periodic wire media. We target a Drude response with a plasma frequency of 22 GHz. To achieve this, the axis of the wires must be parallel to the electric field lines. In the SIW, the electric field in the dominant TE_{10} mode follows lines that meet perpendicularly to the conducting walls of the waveguide (see Fig. 6). According to Ref. [11], the plasma frequency of the array of wires is related to the cell size (the period of the array of wires) T and the radius r of the wire:

$$\omega_p^2 = \frac{2\pi}{\mu_0 \varepsilon_0 T^2 \left[\ln\left\{\frac{T}{2\pi r}\right\} + 0.5275\right]}. \tag{6}$$

A large set of T and r may satisfy this equation but the wire array must be designed to be sufficiently dense to create an effective medium within the available antenna space. The other important constraint is manufacturing, which imposes a lower limit on the wire radius. Here, we estimate that a reasonable value for the radius of metalized vias is

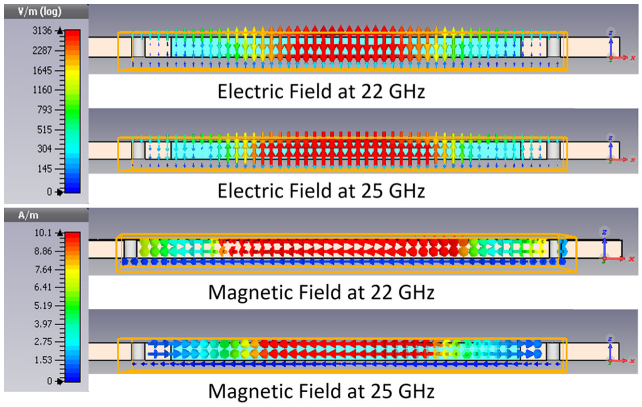

FIG. 6. The electric field distribution: the MTM medium (the MTM is shown in cyan) is modeled by the Drude equation and $f_p = 22$ GHz.

0.15 mm. Therefore, we fix r to 0.15 mm and the proper cell size is found from Eq. (6) to be $T = 2.8$ mm. Figure 7 shows a cell of thin wire. The finite-element-method (FEM) simulation tool CST MICROWAVE is used to simulate and extract the constitutive parameters of the wire. According to this figure, the permittivity of the cell follows the Drude model and the plasma frequency is about 21.5 GHz, as expected. The imaginary part of the permittivity is negligible, consistent with the approximations used to derive Eq. (6). The substrate and metalized via are modeled with corresponding losses: a loss tangent of 0.0012 for the RT5870 and a conductivity of $5.8 \times 10^7 [S/m]$ for copper. According to this figure, the effective refractive index, n_{eff}, of the cell is less than unity over a broad-enough frequency range. Note that the permeability of the effective medium is higher than 2. Although this value is not high enough to miniaturize such a magnetic current antenna, it helps to slightly increase the relative bandwidth [39].

B. Antenna configuration

The antenna comprises three main parts: the main slot radiator, the SIW structure, and the low-index MTM, which is realized by an array of thin wires. The slot radiator is etched by an offset from the substrate edge, L_{offset}. Some SIW metallic vias are located at the edges of a rectangular cavity to prevent any other wave leakage and a set of smaller vias are used to implement the low-index wire medium. Their periodicity and radius are calculated and designed as in Sec. III A. To eliminate any unwanted effects on the antenna input impedance, one of these vias, the nearest to the antenna feed point, is removed. The antenna is printed on Rogers RT5870 substrate with a thickness of 0.787 mm and a relative permittivity of 2.33. A schematic and a photograph of the fabricated antenna are shown in Fig. 8: the design parameters are presented in the figure caption. Two prototypes with different slot widths of

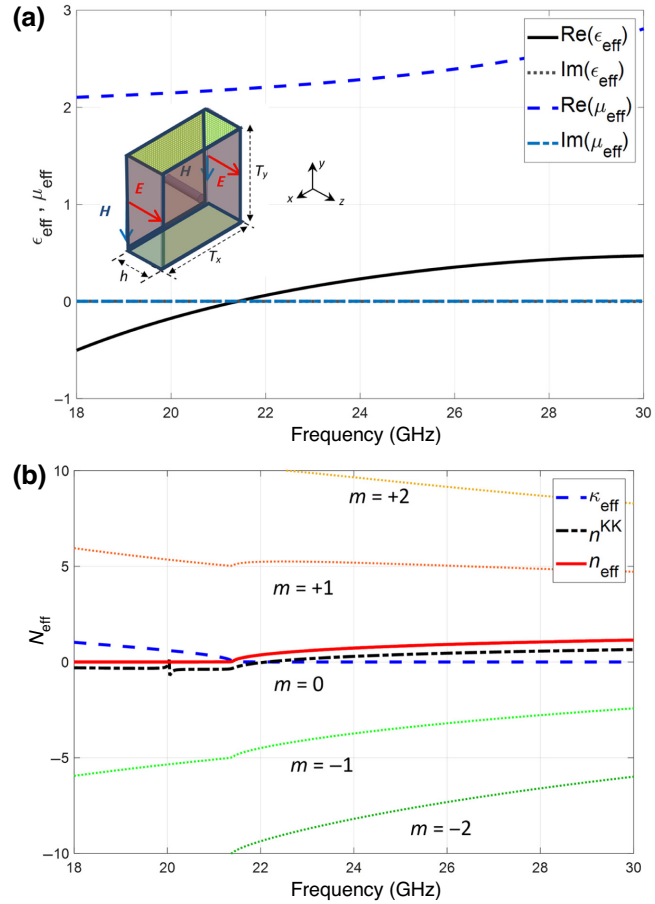

FIG. 7. (a) A schematic of a single cell and the effective permittivity. (b) The refractive index, n_{eff}, versus the frequency. $T = T_x = T_y = 2.8$ mm, $r = 0.15$ mm, and $h = 0.787$ mm.

0.5 and 0.6 mm have been designed and fabricated. A high-frequency 2.92-mm connector is soldered and four solder pads are used to ease this connection.

It is worth noting that we need to consider the effects of the physical connector in the numerical simulations. This assumption becomes crucial when we aim to conduct a fair comparison in measuring the $|S_{11}|$ parameter of the antenna when we have a connector. Nevertheless, in practical scenarios where the antenna is integrated into the front end of the transceiver, certain adjustments to the antenna parameters become imperative in order to achieve the desired broadband performance. Furthermore, taking the connector model into account during numerical simulations has the effect of constraining the bandwidth of the antenna and causing a shift in the radiation pattern of the antenna in the y-z plane.

C. Operation principle

One may wonder whether the bandwidth enhancement results from the combination of the resonant frequency of the slot with the resonant frequencies of the SIW cavity.

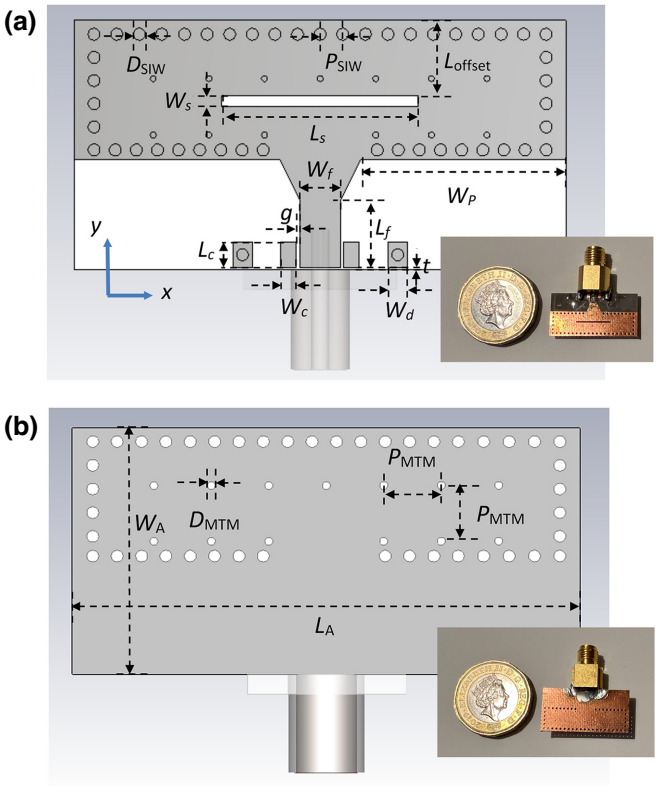

FIG. 8. The (a) front and (b) back view of the antenna schematic and the fabricated prototype. The dimensions are $L_A = 25$, $W_A = 12.5$, $L_S = 10$, $W_f = 2.1$, $L_f = 3.4$, $P_{SIW} = 1.15$, $D_{SIW} = 0.6$, $D_{MTM} = 2r = 0.3$, $P_{MTM} = 2.8$, $W_P = 10.45$, $L_{offset} = 3.8$, $L_c = 1$, $W_c = 0.8$, $W_d = 1.3$, $g = 0.15$, and $t = 0.1$. Design I, $W_s = 0.5$; design II, $W_s = 0.6$; dimensions in millimeters.

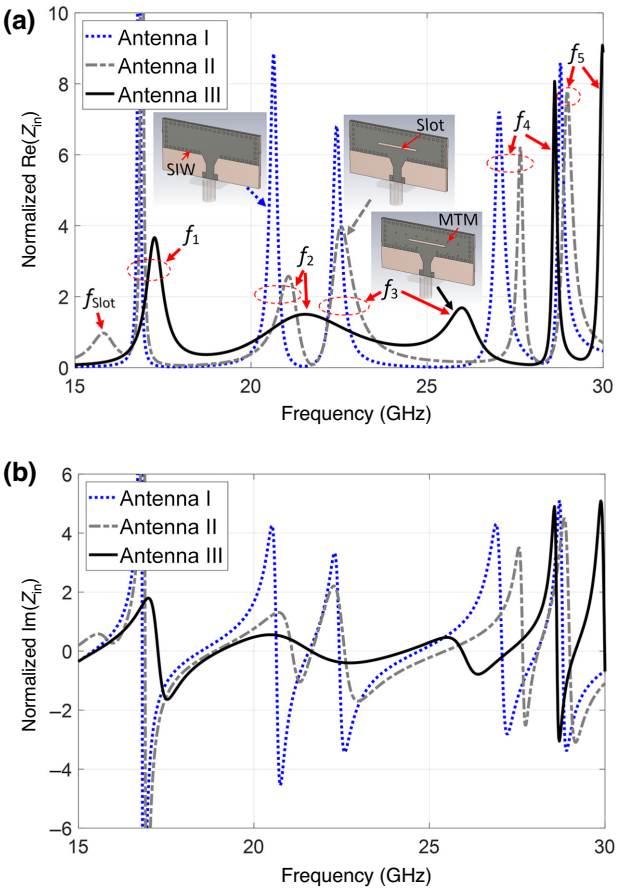

FIG. 9. The normalized input impedance (to 50 Ω) of the SIW cavity (Ant I), the unloaded SIW slot (Ant II), and the proposed antenna (Ant III). The design parameters are presented in Fig. 8.

However, this is not the case. These resonant frequencies are far from each other and the mechanism for bandwidth enhancement is not a resonant interaction with the cavity modes but, rather, a result of the mechanism discussed in the Sec. II. To confirm the operating principle of the antenna, Fig. 9 compares the normalized input impedance of the SIW cavity (Ant I), the SIW slot structure (Ant II), and the proposed antenna (Ant III). The slot length is 10 mm and the diameter, D_{SIW}, and the period, P_{SIW}, of the SIW vias are 0.6 and 1.2, respectively. All three structures have the same dimensions.

The SIW cavity (Ant I) has five distinct resonant frequencies from 15 GHz to 30 GHz, which we have labeled by f_1 to f_5. According to Fig. 2, it has been analytically predicted that the resonant frequency of a 10-mm slot should occur at 16.2 GHz. Adding a slot to the SIW-cavity structure (Ant II), an additional resonant frequency indeed appears at $f_{slot} = 15.8$ GHz (consistent with the analytical result), while the other resonant frequencies—especially f_1, f_2, and f_3—show no considerable change.

Loading the SIW slot with the array of wires (Ant III) has a similar effect on the input impedance, as previously seen in Fig. 2: namely, it decreases the variation of the real and imaginary parts and shifts up the resonant frequencies. It is evident that the slot resonant frequency, f_{slot}, is always far from the SIW-cavity resonant frequencies, f_2 and f_3, and does not fall within their line widths. On the other hand, adding the array of wires increases the distance between these frequencies compared to the unloaded SIW slot antenna, consistent with a change of effective index. This variation is observed to be more significant in f_2 and f_3.

This behavior is more deeply investigated in Fig. 10. This figure compares the normalized input impedance of Ant II and Ant III when the slot length changes from 8 mm to 14 mm. It is clear that the variation of the slot length leads to slight changes in the Ant II resonant frequencies, f_2 and f_3. As a result, one cannot achieve a significant impedance bandwidth by just combining the slot resonant with the SIW-cavity resonant frequencies. Conversely, the low-index wire medium MTM causes a significant decrease in both the real and imaginary parts

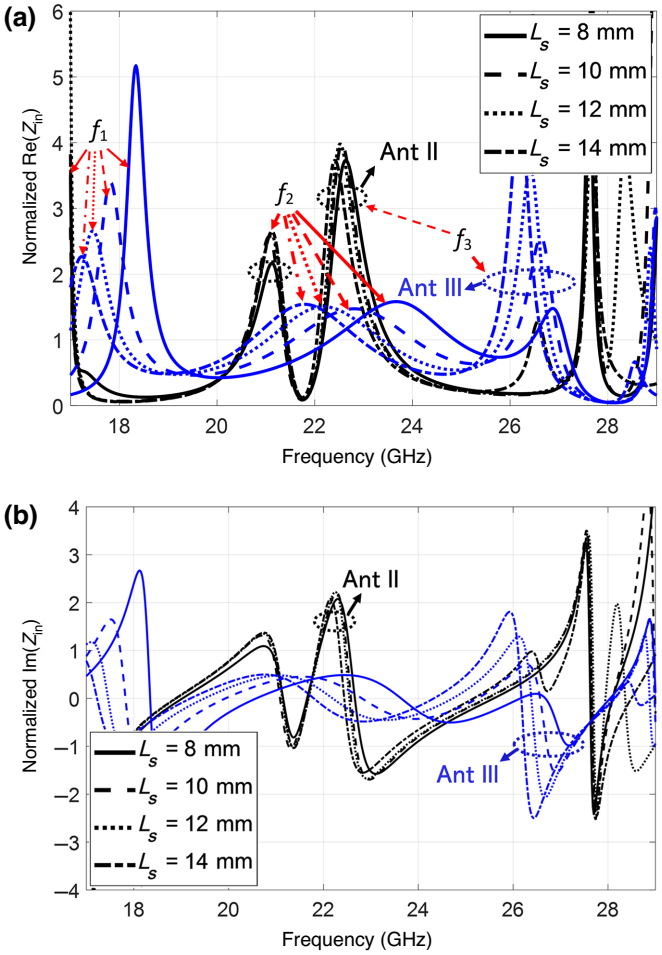

FIG. 10. The normalized input impedance (to 50 Ω) of the unloaded SIW slot (black) and the proposed antenna (blue) when the slot length changes from 8 mm to 14 mm. The design parameters are presented in Fig. 8.

of the input impedance of Ant III over the frequency range of 20–29 GHz. At the same time, it separates the resonant frequencies—especially f_2—further, which helps to obtain broadband behavior.

The antenna normalized input impedance, Z_{11}, as a function of the slot length, L_S, the width, W_S, the periodicity, P_{MTM}, and the diameter of the wires D_{MTM}, is presented in Fig. 11: all parameters are in millimeters. According to this figure, by increasing the slot length, all resonant frequencies, including f_1, f_2, and f_3, are decreased. As a result, the higher and lower operating frequencies of the antenna decrease.

The smaller the width of the slot, the higher its quality factor and, consequently, the smaller is the antenna bandwidth. Thus, increasing the slot width provides a higher operating bandwidth. By increasing the periodicity of the wires from 2.2 to 3.0 mm, the plasma frequency of the effective medium decreases and, accordingly, f_1 and f_3 are reduced. However, this does not lead to a drop in the

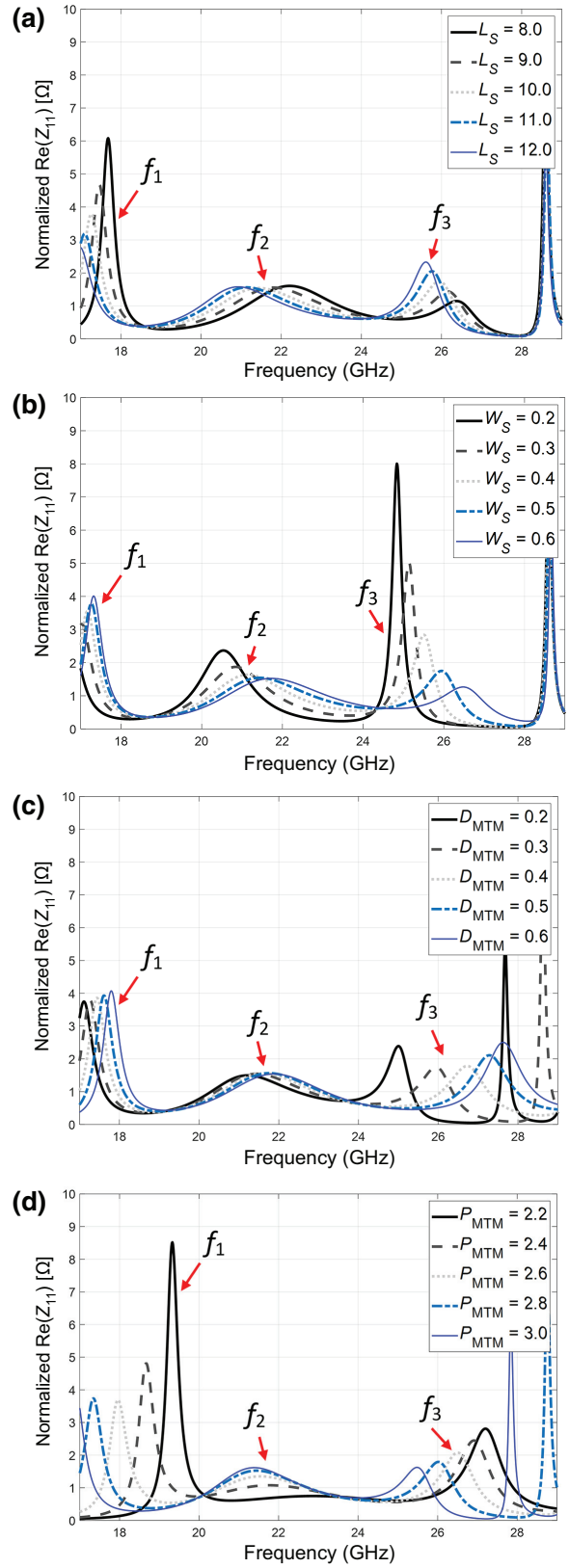

FIG. 11. The normalized input impedance (to 50 Ω) of the antenna as a function of the slot length, L_S, the width, W_S, the periodicity, P_{MTM}, and the diameter of the wires D_{MTM}. All parameters are in millimeters.

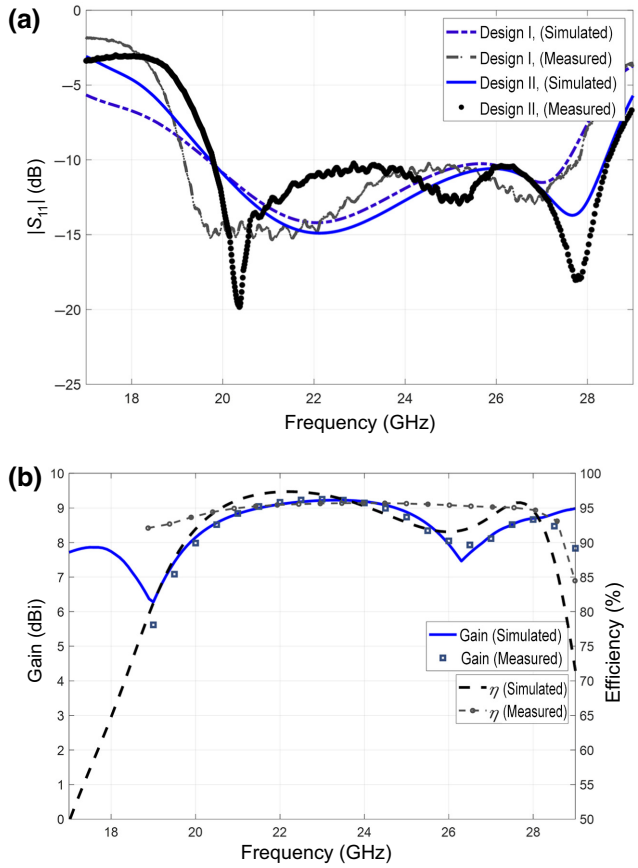

FIG. 12. The simulated and measured (a) $|S_{11}|$ and (b) realized gain and efficiency of the proposed antenna.

antenna operating frequency because of the simultaneous growth of f_2, which compensates for this effect. At a larger wire periodicity, f_2 does not change much but the higher frequency bound can still be decreased, since f_3 still drops when P_{MTM} is increased. Finally, increasing the diameter of the wires causes a significant drop in the higher frequency f_3 of the antenna, while the lower operating frequency f_2 is unaffected.

IV. RESULTS AND DISCUSSION

This section provides simulation and measurement results for the $|S_{11}|$ of both antenna designs. Since the only difference between these designs is the input impedance

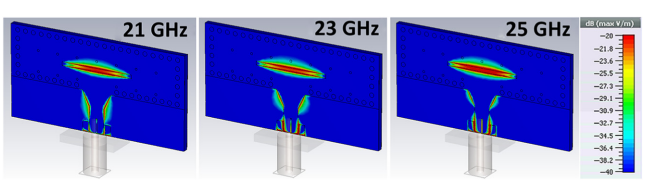

FIG. 13. The electric field distributions at 21, 23, and 25 GHz.

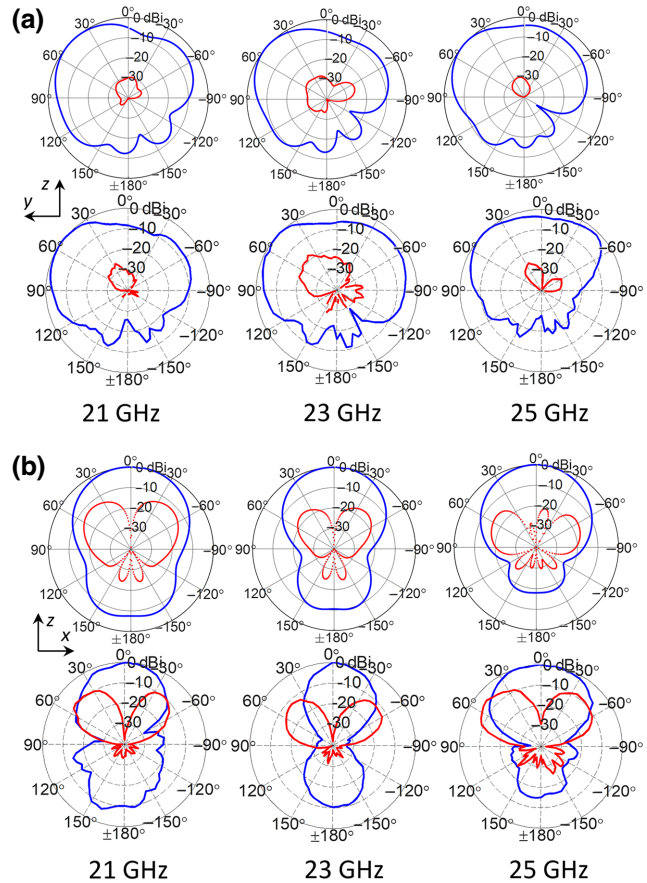

FIG. 14. The simulated and measured normalized radiation patterns at 21 GHz, 23 GHz, and 25 GHz: (a) the y-z plane; (b) the x-z plane. The solid blue pattern corresponds to copolarization and the dotted red pattern depicts cross-polarization.

bandwidth, we will only illustrate the radiation performance and patterns for the first design to keep the presentation concise.

The antenna return loss is measured using an Agilent PNA E8361A network analyzer. Figure 12(a) compares the simulated and measured $|S_{11}|$ for these two designs, indicating acceptable agreement between them. However, some slight differences, especially at lower frequencies, are attributed to the physical realization of the connector and other practical imperfections. In the first design, the antenna operates through a wide bandwidth of 8.1 GHz, starting from 19.7 GHz and extending to 27.8 GHz. According to Fig. 11, increasing the slot width leads to an improved antenna bandwidth. The measurement confirms the expected enhancement and shows a broad impedance bandwidth ($|S_{11}| < -10$ dB) of 36.2% in design II, covering the mmWave frequency range of 19.7–28.4 GHz that could be employed in ISM and/or automotive radar (24.125–24.25 GHz) and 5G (24.25–28.35 GHz) mmWave applications. The simulated and measured realized gain and efficiency of the antenna are compared in Fig. 12(b).

TABLE I. A comparison of the recently published broadband SIW slot antennas: deficiencies are specified in bold type.

Antenna	Frequency (GHz)	Maximum gain (dBi)	η (%)	Bandwidth (%)	Layers	Size (λ)
Ref. [40]	18.2–23.8	9.5	···	26.7	1	$1.51 \times 1.21 \times 0.05$
Ref. [41]	24–29.3 and 35.5–43.5	6.1 and 8.7	···	19.9 and 20.2	**2**	$\mathbf{0.69 \times 0.69 \times 0.17}$
Ref. [42]	26.2–31.2	4.3	···	17.4	**4**	$\mathbf{0.96 \times 0.47 \times 0.24}$
Ref. [43]	24.25–29.5	7.4	85	26.8	**4**	$\mathbf{0.48 \times 0.48 \times 0.09}$
Ref. [44]	23.5–31.5	8.9	90	25.8	**4**	$\mathbf{1.17 \times 1.17 \times 0.09}$
This work	19.7–28.4	9.1	>90	36.2	1	$1.64 \times 0.82 \times 0.05$

According to this figure, the radiation efficiency is above 90%, while the antenna gain is at least 7.5 dBi over the entire operating bandwidth.

The electric field distributions of the antenna at 21, 23, and 25 GHz are presented in Fig. 13. It is evident that the electric field distribution is not changed considerably versus the frequency. This confirms that the radiation mechanism of the antenna is stable over the operating bandwidth. Figure 14 illustrates the x-z and y-z planes of the measured and simulated normalized radiation patterns at 21, 23, and 25 GHz. According to this figure, the antenna main lobe in the y-z plane deviates from the broadside; this slant radiation relates to the feeding mechanism and the leaky-wave behavior of the low-index effective medium. This deviation is not desirable in some practical applications; however, it is absolutely crucial in portable or fixed cellular communications. Since the slot antenna is printed on a compact single-layer substrate, the back radiation of such a finite ground structure is inevitable. It is worth noting that one can simply apply the conventional back-radiation reduction methods to the proposed antenna (e.g., cavity back, stack structure, etc.), which is beyond the scope of this paper. The results show that the antenna radiation does not significantly change over the operating frequency. The antenna exhibits a high polarization discrimination of -20 dB in the main lobe. However, due to the presence of the dielectric and the low height of the SIW technology, a comparably higher cross-polarization in the other direction, especially in the x-z plane, is observed.

Table I compares the proposed antenna performance with recently published papers. In this table, deficiencies are specified in bold type. Note that the manufacturing cost of a multilayer structure is significantly higher than that of a single-layer structure. The antenna dimensions are 25×12.5 mm^2. It provides a higher fractional bandwidth (36.2%), while its electrical size is compact. Additionally, the antenna has a higher gain compared to other single-SIW slot antennas. This is mainly due to the lower electrical permittivity of the MTM substrate.

It should be noted that the guided wavelength of a SIW slot is inversely related to the substrate permittivity, $\lambda_g \propto 1/\sqrt{\epsilon}$ [45]. Although it is expected that the size of the radiating element will increase by reducing ϵ, the impedance bandwidth and the electrical size of the proposed antenna are mainly defined by the resonant frequencies of the SIW structure rather than the radiating slot (which resonates at 15.8 GHz). As a result, we have been able to achieve, simultaneously, a compact low-profile and broadband behavior of both the impedance matching and the radiation efficiency. The overall dimensions of the antenna are approximately $1.64\lambda_L \times 0.82\lambda_L \times 0.05\lambda_L$ ($f_L = 19.7$ GHz and λ_L is the free-space wavelength corresponding to the lower frequency).

V. CONCLUSIONS

In this paper, we have introduced a technique to enhance the impedance bandwidth of the SIW slot antenna. It has been shown that an array of thin wires effectively realizes a low-index medium and such an MTM improves the antenna radiation and the impedance bandwidth simultaneously. The measurements indicate a 36.2% fractional bandwidth, over 8.7 GHz, which is drastically boosted when compared to the conventional unloaded slot antenna. The performance of the fabricated antenna agrees well with the simulations, expressing the same frequency bandwidth. The antenna provides an average gain of 8.5 dBi, while the radiation efficiency remains above 90% over the entire operating-frequency band, from 19.7 to 28.4 GHz. The proposed antenna not only has a broad impedance bandwidth but also an improved radiation bandwidth.

[1] S. Liao, P. Chen, P. Wu, K. M. Shum, and Q. Xue, Substrate-integrated waveguide-based 60-GHz resonant slotted waveguide arrays with wide impedance bandwidth and high gain, IEEE Trans. Antennas Propag. **63**, 2922 (2015).

[2] Y.-Q. Wen, B.-Z. Wang, and X. Ding, Wide-beam SIW-slot antenna for wide-angle scanning phased array, IEEE Antennas Wirel. Propag. Lett. **15**, 1638 (2016).

[3] T. Deckmyn, S. Agneessens, A. C. F. Reniers, A. B. Smolders, M. Cauwe, D. Vande Ginste, and H. Rogier, A novel 60 GHz wideband coupled half-mode/quarter-mode substrate integrated waveguide antenna, IEEE Trans. Antennas Propag. **65**, 6915 (2017).

[4] P. N. Choubey, W. Hong, Z.-C. Hao, P. Chen, T.-V. Duong, and J. Mei, A wideband dual-mode SIW cavity-backed triangular-complimentary-split-ring-slot (TCSRS) antenna, IEEE Trans. Antennas Propag. **64**, 2541 (2016).
[5] X. Cheng, Y. Yao, J. Yu, and X. Chen, Circularly polarized substrate-integrated waveguide tapered slot antenna for millimeter-wave applications, IEEE Antennas Wirel. Propag. Lett. **16**, 2358 (2017).
[6] G.-H. Sun and H. Wong, A planar millimeter-wave antenna array with a pillbox-distributed network, IEEE Trans. Antennas Propag. **68**, 3664 (2020).
[7] J. Xu, W. Hong, Z. H. Jiang, and H. Zhang, Millimeter-wave broadband substrate integrated magneto-electric dipole arrays with corporate low-profile microstrip feeding structures, IEEE Trans. Antennas Propag. **68**, 7056 (2020).
[8] M. K. Moghaddam and R. Fleury, Subwavelength metawaveguide filters and metaports, Phys. Rev. Appl. **16**, 044010 (2021).
[9] Z. Zhang, P. Delplace, and R. Fleury, Anomalous topological waves in strongly amorphous scattering networks, Sci. Adv. **9**, eadg3186 (2023).
[10] A. Jafargholi and A. Jafargholi, Miniaturisation of printed slot antennas using artificial magnetic conductors, IET Microw. Antennas Propag. **12**, 1054 (2018).
[11] N. Engheta and R. W. Ziolkowski. *Metamaterials: Physics and Engineering Explorations* (IEEE Press, Piscataway, NJ, 2006).
[12] S. S. Mousavi Khaleghi, G. Moradi, R. Sarraf Shirazi, and A. Jafargholi, Microstrip line impedance matching using ENZ metamaterials, design, and application, IEEE Trans. Antennas Propag. **67**, 2243 (2019).
[13] B. A. Esmail, S. Koziel, L. Golunski, H. B. A. Majid, and R. K. Barik, Overview of metamaterials-integrated antennas for beam manipulation applications: The two decades of progress, IEEE Access **10**, 67096 (2022).
[14] V. Torres, B. Orazbayev, V. Pacheco-Peña, J. Teniente, M. Beruete, M. Navarro-Cía, M. S. Ayza, and N. Engheta, Experimental demonstration of a millimeter-wave metallic ENZ lens based on the energy squeezing principle, IEEE Trans. Antennas Propag. **63**, 231 (2014).
[15] D. Ramaccia, F. Scattone, F. Bilotti, and A. Toscano, Broadband compact horn antennas by using EPS-ENZ metamaterial lens, IEEE Trans. Antennas Propag. **61**, 2929 (2013).
[16] D. Ramaccia, M. Barbuto, A. Monti, A. Verrengia, F. Trotta, D. Muha, S. Hrabar, F. Bilotti, and A. Toscano, Exploiting intrinsic dispersion of metamaterials for designing broadband aperture antennas: Theory and experimental verification, IEEE Trans. Antennas Propag. **64**, 1141 (2016).
[17] S. Zhong, J. Feng, Z.-W. Zheng, and Y. Ma, Ultrathin and simple 3-D rasorber based on ferrites with embedded epsilon-near-zero waveguides, IEEE Antennas Wirel. Propag. Lett. **21**, 1896 (2022).
[18] R. Dehbashi, K. S. Bialkowski, and A. M. Abbosh, Size reduction of electromagnetic devices using double near-zero materials, IEEE Trans. Antennas Propag. **65**, 7102 (2017).
[19] K. Wei and A. Zhang, Meta-antennas: From academic research to industrial applications of mobile terminals [Industry activities], IEEE Antennas Propag. Mag. **64**, 167 (2022).
[20] N. Vojnovic, B. Jokanovic, M. Radovanovic, F. Medina, and F. Mesa, Modeling of nonresonant longitudinal and inclined slots for resonance tuning in ENZ waveguide structures, IEEE Trans. Antennas Propag. **63**, 5107 (2015).
[21] M. Mitrovic, B. Jokanovic, and N. Vojnovic, Wideband tuning of the tunneling frequency in a narrowed epsilon-near-zero channel, IEEE Antennas. Wirel. Propag. Lett. **12**, 631 (2013).
[22] H. Li, Z. Zhou, and Y. Li, Length-irrelevant dual-polarized antenna based on antiphase epsilon-near-zero mode, IEEE Trans. Antennas Propag. **70**, 720 (2021).
[23] J. Xiong, X. Lin, Y. Yu, M. Tang, S. Xiao, and B. Wang, Novel flexible dual-frequency broadside radiating rectangular patch antennas based on complementary planar ENZ or MNZ metamaterials, IEEE Trans. Antennas Propag. **60**, 3958 (2012).
[24] J. Long, M. M. Jacob, and D. F. Sievenpiper, Broadband fast-wave propagation in a non-Foster circuit loaded waveguide, IEEE Trans. Microw. Theory Tech. **62**, 789 (2014).
[25] J. Long and D. F. Sievenpiper, The observation of dispersionless superluminal propagation in a non-Foster loaded waveguide and its fundamental limitations, IEEE Trans. Microw. Theory Tech. **66**, 762 (2017).
[26] D. F. Sievenpiper, Superluminal waveguides based on non-Foster circuits for broadband leaky-wave antennas, IEEE Antennas Wirel. Propag. Lett. **10**, 231 (2011).
[27] M. M. Jacob, J. Long, and D. F. Sievenpiper, Non-Foster loaded parasitic array for broadband steerable patterns, IEEE Trans. Antennas Propag. **62**, 6081 (2014).
[28] A. Jafargholi and M. H. Mazaheri, Broadband microstrip antenna using epsilon near zero metamaterials, IET Microw. Antennas Propag. **9**, 1612 (2015).
[29] A. Dadgarpour, M. S. Sorkherizi, T. A. Denidni, and A. A. Kishk, Passive beam switching and dual-beam radiation slot antenna loaded with ENZ medium and excited through ridge gap waveguide at millimeter-waves, IEEE Trans. Antennas Propag. **65**, 92 (2016).
[30] E. Forati, G. W. Hanson, and D. F. Sievenpiper, An epsilon-near-zero total-internal-reflection metamaterial antenna, IEEE Trans. Antennas Propag. **63**, 1909 (2015).
[31] J. C. Soric, N. Engheta, S. Maci, and A. Alu, Omnidirectional metamaterial antennas based on ε-near-zero channel matching, IEEE Trans. Antennas Propag. **61**, 33 (2013).
[32] Z. Liu, Z. Zhou, Y. Li, and Y. Li, Integrated epsilon-near-zero antenna for omnidirectional radiation, Appl. Phys. Lett. **119**, 151904 (2021).
[33] S. S. Al-Bawri, M. T. Islam, T. Shabbir, G. Muhammad, M. S. Islam, and H. Y. Wong, Hexagonal shaped near zero index (NZI) metamaterial based MIMO antenna for millimeter-wave application, IEEE Access **8**, 181003 (2020).
[34] Z. Zhou and Y. Li, A photonic-doping-inspired SIW antenna with length-invariant operating frequency, IEEE Trans. Antennas Propag. **68**, 5151 (2020).
[35] Z. Zhou and Y. Li, Effective epsilon-near-zero (ENZ) antenna based on transverse cutoff mode, IEEE Trans. Antennas Propag. **67**, 2289 (2019).

[36] Z. Hu, C. Chen, Z. Zhou, and Y. Li, An epsilon-near-zero-inspired pdms substrate antenna with deformation-insensitive operating frequency, IEEE Antennas Wirel. Propag. Lett. **19**, 1591 (2020).

[37] L. Yousefi and O. Ramahi, Miniaturised antennas using artificial magnetic materials with fractal Hilbert inclusions, Electron. Lett. **46**, 816 (2010).

[38] R. W. Larson and V. M. Powers, Slots in dielectrically loaded waveguide, Radio Sci. **1**, 31 (1966).

[39] A. O. Karilainen, P. M. T. Ikonen, C. R. Simovski, and S. A. Tretyakov, Choosing dielectric or magnetic material to optimize the bandwidth of miniaturized resonant antennas, IEEE Trans. Antennas Propag. **59**, 3991 (2011).

[40] T. Cheng, W. Jiang, S. Gong, and Y. Yu, Broadband SIW cavity-backed modified dumbbell-shaped slot antenna, IEEE Antennas Wirel. Propag. Lett. **18**, 936 (2019).

[41] S. Ni, X. Li, X. Qiao, Q. Wang, and J. Zhang, A compact dual-wideband magnetoelectric dipole antenna for 5G millimeter-wave applications, IEEE Trans. Antennas Propag. **70**, 9112 (2022).

[42] M. F. Khajeim, G. Moradi, R. S. Shirazi, S. Zhang, and G. F. Pedersen, Wideband vertically polarized antenna with endfire radiation for 5G mobile phone applications, IEEE Antennas Wirel. Propag. Lett. **19**, 1948 (2020).

[43] I. Lima de Paula, S. Lemey, D. Bosman, Q. Van den Brande, O. Caytan, J. Lambrecht, M. Cauwe, G. Torfs, and H. Rogier, Cost-effective high-performance air-filled SIW antenna array for the global 5G 26 GHz and 28 GHz bands, IEEE Antennas Wirel. Propag. Lett. **20**, 194 (2021).

[44] H.-T. Hu and C. H. Chan, Substrate-integrated-waveguide-fed wideband filtering antenna for millimeter-wave applications, IEEE Trans. Antennas Propag. **69**, 8125 (2021).

[45] J. E. Rayas-Sanchez and V. Gutierrez-Ayala, in *2008 IEEE MTT-S International Microwave Symposium Digest* (Atlanta, GA, USA, 2008), p. 983.